Mechanical modeling of helical structures accounting for translational invariance. Part 1: Static behavior

Ahmed Frikha, Patrice Cartraud, Fabien Treyssede

Mechanical modeling of helical structures accounting for translational invariance. Part 1: Static behavior

Ahmed Frikha[a], Patrice Cartraud[b], Fabien Treyssède[a,*]

[a] *LUNAM Université, IFSTTAR, MACS, F-44344 Bouguenais, France*
[b] *LUNAM Université, GeM, UMR CNRS 6183, Ecole Centrale de Nantes, 1 rue de la Noë, 44 321 Nantes Cédex 3, France*

Abstract

The purpose of this paper is to investigate the static behavior of helical structures under axial loads. Taking into account their translational invariance, the homogenization theory is applied. This approach, based on asymptotic expansion, gives the first-order approximation of the 3D elasticity problem from the solution of a 2D microscopic problem posed on the cross-section and a 1D macroscopic problem, which turns out to be a Navier-Bernoulli-Saint-Venant beam problem. By contrast with earlier references in which a reduced 3D model was built on a slice of the helical structure, the contribution of this paper is to propose a 2D microscopic model. Homogenization is first applied to helical single wire structures, i.e. helical springs. Next, axial elastic properties of a seven-wire strand are computed. The approach is validated through comparison with reference results: analytical solution for helical single wire structures and 3D detailed finite element solution for seven-wire strands.

Keywords: Homogenization; Helical coordinates; Finite element method; Helical springs; Seven-wire strands; Axial load.

1. Introduction

Helical structures are widely used in mechanical and civil engineering applications. These structures are usually subjected to large loads which can lead

*Corresponding author
Email address: fabien.treyssede@ifsttar.fr (Fabien Treyssède)

to the material degradation and cracks associated with corrosion and mechanical fatigue. This threatens the structural strength. In this framework, non-destructive testing is a crucial tool for detection, localisation and measurement of material discontinuities. The choice of the appropriate technique depends on dimensions and accessibility of the structure. Particularly, ultrasonics allow to control large components, such as plates and tubes, by analyzing their elastic guided waves. The purpose of this study, which is composed of two parts, is to develop a numerical model for the analysis of the elastic wave propagation phenomenon in prestressed helical structures. This problem requires the computation of the static prestress state. Therefore, a first model will be developed in Part 1 of this paper, to compute this static state. Taking into account this prestress state, a second model will be developed in Part 2, in order to analyze the wave propagation in these prestressed structures. The goal of this first part of this paper is thus to develop an approach that allows the computation of the prestress state in helical structures subjected to axial load.

Numerous works have been devoted to the modeling of the static behavior of helical structures as springs and multi-wire cables under axial loads. For helical springs, an analytical model was proposed among others in Ancker and Goodier (1958) and Wahl (1963) considering the spring as an Euler-Bernoulli beam with pitch and curvature corrections. Numerical approaches describing the static behavior of helical springs have been also developed. Among these works, a finite element model of half of a spring slice has been proposed in Jiang and Henshall (2000).

The static behavior of seven-wire strands has been widely studied in literature. Various analytical models based on different assumptions have been proposed, such as the model of Costello (1977) which is one of the most popular. These models are reviewed in Jolicoeur and Cardou (1991) and compared in Jolicoeur and Cardou (1991) and Ghoreishi et al. (2007). Besides, numerical models relying on the finite element method were developed. Some of them are based on beam elements (Durville (1998); Nawrocki and Labrosse (2000); Páczelt and Beleznai (2011)), see also Nemov et al. (2010) and Bajas et al.

(2010) in which ITER superconducting cables composed of a large number of strands are studied. But most of the time, 3D models are used, see e.g. Boso et al. (2006), Ghoreishi et al. (2007), İmrak and Erdönmez (2010), Nemov et al. (2010), Stanova et al. (2011a,b), Erdönmez and İmrak (2011). In order to obtain a good representation of the geometry as well as the displacement solution, which may involve bending phenomena, quadratic elements are employed. This leads to models which can be computationally expensive, when the model axial length is about the pitch length. Therefore, as soon as the loading fulfills helical symmetry, one can take benefit of this property to reduce the model size. This has been achieved in Jiang et al. (1999, 2008) in which the computational domain is restricted to a basic sector of a helical slice. Helical symmetry may also be accounted for within the framework of homogenization theory. This has been proposed first in Cartraud and Messager (2006) using axial periodicity, and then improved in Messager and Cartraud (2008), in which helical symmetry enables to consider one slice of a strand. The derivation of the slice model is different in Jiang et al. (1999, 2008) and Messager and Cartraud (2008). However, in both cases, helical symmetry yields displacement constraints between the two faces of the slice, with a loading under the form of an axial strain and a twist rate.

This work further advances Cartraud and Messager (2006) and Messager and Cartraud (2008), taking advantage of the translational invariance. Helical symmetry can be actually considered more efficiently. Thus the model can be reduced to a 2D one, i.e. a cross-section model. This requires to formulate the homogenization theory in a twisted coordinate system. This technique then allows the computation of the static prestressed state of helical structures (single wire and multi-wire) from the solution of a 2D problem. Let us mention that an advanced analytical 2D model has been recently proposed in Argatov (2011). This model takes into account Poisson's effect, contact deformation and allows to obtain the overall strand stiffness as well as local contact stresses. In this reference, plane strain was assumed to formulate the 2D problem while in the present work helical symmetry is used.

The method developed in this paper is restricted to multi-wire helical struc-

tures composed of a stack of helical wires wrapped with the same twisting rate around a straight axis. As explained in Section 3, this excludes the case of double helical structures (such as independent wire rope core for instance) and cross-lay strands.

This paper is organized as follows. First, in Section 2, the curvilinear coordinate system is introduced. Then in Section 3 the translational invariance is defined, which is a necessary condition for the helical homogenization approach. Based on the asymptotic expansion method and exploiting the translational invariance property, the homogenization procedure is presented in Section 4. Its finite element solution is detailed in Section 5. The helical homogenization approach is validated for helical single wire and seven-wire structures by comparison with analytical or numerical models in Section 6.

2. Curvilinear coordinate system

A helical structure is considered (see Fig.1). Let $(\mathbf{e}_X, \mathbf{e}_Y, \mathbf{e}_Z)$ its Cartesian orthonormal basis. The helix centreline is defined by its helix radius R in the Cartesian plane $(\mathbf{e}_X, \mathbf{e}_Y)$ and the length of one helix pitch along the Z-axis denoted by L. This helix centerline can be described by the following position vector:

$$\mathbf{r}(s) = R\cos(\frac{2\pi}{l}s + \theta)\mathbf{e}_X + R\sin(\frac{2\pi}{l}s + \theta)\mathbf{e}_Y + \frac{L}{l}s\mathbf{e}_Z, \tag{1}$$

where $l = \sqrt{L^2 + 4\pi^2R^2}$ is the curvilinear length of one helix pitch and θ is the helix phase angle in the $Z = 0$ plane. For a seven-wire strand, θ is equal to $(N-1)\pi/3$, where $N = 1, .., 6$ refers to the number of the helical wire. θ is equal to zero for a single wire helical structure. The helix lay angle Φ is defined by $\tan\Phi = 2\pi R/L$. A complete helix is described by the parameter s varying from 0 to l.

2.1. Serret-Frenet basis

A Serret-Frenet basis $(\mathbf{e}_n, \mathbf{e}_b, \mathbf{e}_t)$ associated to the helix can be defined (see e.g. Gray et al. (2006)), where the unit vectors $\mathbf{e}_n$, $\mathbf{e}_b$, $\mathbf{e}_t$ are given by $\mathbf{e}_t = d\mathbf{r}/ds$,

$d\mathbf{e}_n/ds = \tau\mathbf{e}_b - \kappa\mathbf{e}_t$ and $d\mathbf{e}_b/ds = -\tau\mathbf{e}_n$. For helical curves, the curvature $\kappa = 4\pi^2 R/l^2$ and the torsion $\tau = 2\pi L/l^2$ are constant. In the Cartesian basis, $\mathbf{e}_n$, $\mathbf{e}_b$ and $\mathbf{e}_t$ are expressed by:

$$\begin{aligned}
\mathbf{e}_n &= -\cos(\frac{2\pi}{l}s+\theta)\mathbf{e}_X - \sin(\frac{2\pi}{l}s+\theta)\mathbf{e}_Y \ , \\
\mathbf{e}_b &= \frac{L}{l}\sin(\frac{2\pi}{l}s+\theta)\mathbf{e}_X - \frac{L}{l}\cos(\frac{2\pi}{l}s+\theta)\mathbf{e}_Y + \frac{2\pi}{l}R\mathbf{e}_Z \ , \\
\mathbf{e}_t &= -\frac{2\pi R}{l}\sin(\frac{2\pi}{l}s+\theta)\mathbf{e}_X + \frac{2\pi R}{l}\cos(\frac{2\pi}{l}s+\theta)\mathbf{e}_Y + \frac{L}{l}\mathbf{e}_Z.
\end{aligned} \tag{2}$$

The normal vector $\mathbf{e}_n$ remains parallel to the $(\mathbf{e}_X, \mathbf{e}_Y)$ plane while $\mathbf{e}_b$ and $\mathbf{e}_t$ move in the three directions of the Cartesian basis as s and θ vary.

2.2. Twisted basis

A special case of the Serret-Frenet basis denoted by $(\mathbf{e}_x, \mathbf{e}_y, \mathbf{e}_Z)$ corresponding to $\kappa = 0$ and $\tau = 2\pi/L$ can be considered. It corresponds to a twisted coordinate system along the Z-axis ($s \equiv Z$) with axial periodicity L. The unit vectors $\mathbf{e}_x$ and $\mathbf{e}_y$ rotate around the Z-axis and remain parallel to the $(\mathbf{e}_X, \mathbf{e}_Y)$ plane (see Fig. 1). In the Cartesian basis, $\mathbf{e}_x$ and $\mathbf{e}_y$ are expressed as:

$$\begin{aligned}
\mathbf{e}_x &= -\cos(\frac{2\pi}{L}Z+\theta)\mathbf{e}_X - \sin(\frac{2\pi}{L}Z+\theta)\mathbf{e}_Y \ , \\
\mathbf{e}_y &= \sin(\frac{2\pi}{L}Z+\theta)\mathbf{e}_X - \cos(\frac{2\pi}{L}Z+\theta)\mathbf{e}_Y.
\end{aligned} \tag{3}$$

It should also be noted that this twisted coordinate system coincides with the one proposed in Onipede and Dong (1996), Nicolet et al. (2004), Nicolet and Zola (2007) for the analysis of twisted and helical structures.

2.3. Covariant and contravariant bases

Differential operators can not be expressed directly in the Serret-Frenet or twisted bases. They have first to be expressed in the covariant and contravariant bases. The reader can find an in-depth treatment of curvilinear coordinate systems in Chapelle and Bathe (2003), Synge and Schild (1978), Wempner (1981) for instance.

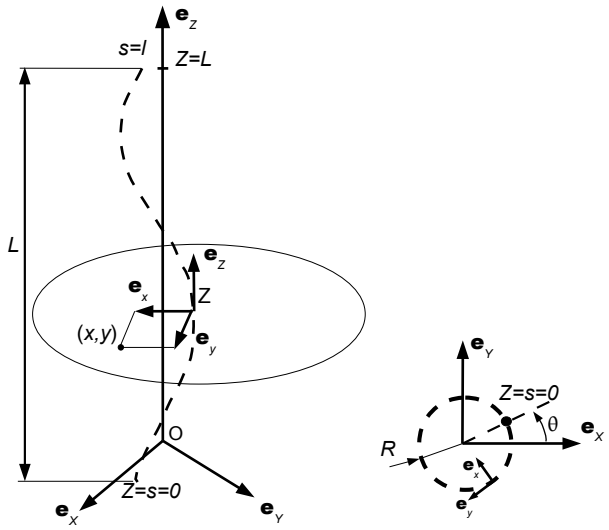

Figure 1: Left: One helix pitch and its twisted basis associated to the twisted coordinate system (x, y, Z). Right: view normal to the Z-axis. The point $Z = s = 0$ lies in the $(\mathbf{e}_X, \mathbf{e}_Y)$ plane.

From the twisted basis $(\mathbf{e}_x, \mathbf{e}_y, \mathbf{e}_Z)$, a new coordinate system (x, y, Z) is built, for which any position vector can be expressed as:

$$\mathbf{X}(x, y, Z) = x\mathbf{e}_x(Z) + y\mathbf{e}_y(Z) + Z\mathbf{e}_Z. \tag{4}$$

The covariant basis $(\mathbf{g}_1, \mathbf{g}_2, \mathbf{g}_3)$ is obtained from the position vector by $(\mathbf{g}_1, \mathbf{g}_2, \mathbf{g}_3) = (\partial\mathbf{X}/\partial x, \partial\mathbf{X}/\partial y, \partial\mathbf{X}/\partial Z)$, which yields in the twisted basis:

$$\begin{aligned} \mathbf{g}_1 = \mathbf{e}_x(Z)\ ,\ \mathbf{g}_2 = \mathbf{e}_y(Z)\ , \\ \mathbf{g}_3 = -\tau y\mathbf{e}_x(Z) + \tau x\mathbf{e}_y(Z) + \mathbf{e}_Z. \end{aligned} \tag{5}$$

Note that the covariant basis is not orthogonal.

The covariant metric tensor, defined by $g_{mn} = \mathbf{g}_m \cdot \mathbf{g}_n$, is then given by:

$$\mathbf{g} = \begin{bmatrix} 1 & 0 & -\tau y \\ 0 & 1 & \tau x \\ -\tau y & \tau x & \tau^2(x^2 + y^2) + 1 \end{bmatrix}. \tag{6}$$

The covariant basis gives rise to the contravariant one $(\mathbf{g}^1, \mathbf{g}^2, \mathbf{g}^3)$, defined from $\mathbf{g}_i \cdot \mathbf{g}^j = \delta_i^j$. Superscripts and subscripts refer to the covariant and contravariant vectors, respectively. $\mathbf{g}^1$, $\mathbf{g}^2$ and $\mathbf{g}^3$ are expressed in the twisted basis as:

$$\mathbf{g}^1 = \mathbf{e}_x(Z) + \tau y \mathbf{e}_Z \ , \ \mathbf{g}^2 = \mathbf{e}_y(Z) - \tau x \mathbf{e}_Z \ , \ \mathbf{g}^3 = \mathbf{e}_Z. \tag{7}$$

The Christoffel symbol of the second kind Γ_{ij}^k, defined by $\Gamma_{ij}^k = \mathbf{g}_{i,j} \cdot \mathbf{g}^k$, can be calculated from the covariant and contravariant bases, which leads to:

$$\begin{aligned} \Gamma_{11}^k = \Gamma_{12}^k = \Gamma_{21}^k = \Gamma_{22}^k = 0, \\ \Gamma_{13}^1 = \Gamma_{31}^1 = 0, \Gamma_{23}^1 = \Gamma_{32}^1 = -\tau, \Gamma_{33}^1 = -\tau^2 x, \\ \Gamma_{23}^2 = \Gamma_{32}^2 = 0, \Gamma_{33}^2 = -\tau^2 y, \Gamma_{13}^2 = \Gamma_{31}^2 = \tau, \\ \Gamma_{13}^3 = \Gamma_{31}^3 = \Gamma_{23}^3 = \Gamma_{32}^3 = \Gamma_{33}^3 = 0. \end{aligned} \tag{8}$$

It is noteworthy that the coefficients Γ_{ij}^k do not depend on the axial variable Z. As shown in the next section, this is a necessary condition for translational invariance.

2.4. Strain tensor

The strain tensor is now rewritten in the curvilinear coordinate system. In the contravariant basis, the strain-displacement relation is (Chapelle and Bathe (2003)):

$$\boldsymbol{\epsilon} = \epsilon_{ij} \mathbf{g}^i \otimes \mathbf{g}^j \ , \ \epsilon_{ij} = \frac{1}{2}(u_{i,j} + u_{j,i}) - \Gamma_{ij}^k u_k, \tag{9}$$

where the u_i's denote the displacement covariant components.

Using the relation (7) between the contravariant and the twisted bases, the strain vector can then be expressed in the twisted basis as follows:

$$\{\epsilon\} = (\mathbf{L}_{xy} + \mathbf{L}_Z \frac{\partial}{\partial Z})\{u\},$$

$$\mathbf{L}_{xy} = \begin{bmatrix} \partial/\partial x & 0 & 0 \\ 0 & \partial/\partial y & 0 \\ 0 & 0 & \Lambda \\ \partial/\partial y & \partial/\partial x & 0 \\ \Lambda & -\tau & \partial/\partial x \\ \tau & \Lambda & \partial/\partial y \end{bmatrix}, \mathbf{L}_Z = \begin{bmatrix} 0 & 0 & 0 \\ 0 & 0 & 0 \\ 0 & 0 & 1 \\ 0 & 0 & 0 \\ 1 & 0 & 0 \\ 0 & 1 & 0 \end{bmatrix}, \tag{10}$$

where $\Lambda = \tau(y\partial/\partial x - x\partial/\partial y)$. The column vectors $\{u\} = [u_x\, u_y\, u_Z]^T$ and $\{\epsilon\} = [\epsilon_{xx}\, \epsilon_{yy}\, \epsilon_{ZZ}\, 2\epsilon_{xy}\, 2\epsilon_{xZ}\, 2\epsilon_{yZ}]^T$ are the displacement vector and the strain vector respectively, both written in the orthonormal twisted basis $(\mathbf{e}_x, \mathbf{e}_y, \mathbf{e}_Z)$.

2.5. Constitutive law

For an isotropic material, the elasticity tensor is given in the covariant basis by (Chapelle and Bathe (2003)):

$$\begin{aligned} \mathbf{C} &= C^{ijkl}\mathbf{g}_i \otimes \mathbf{g}_j \otimes \mathbf{g}_k \otimes \mathbf{g}_l, \\ C^{ijkl} &= \frac{\nu E}{(1+\nu)(1-2\nu)} g^{ij}g^{kl} + \frac{E}{2(1+\nu)}(g^{ik}g^{jl} + g^{il}g^{jk}), \end{aligned} \tag{11}$$

where E and ν are the Young modulus and the Poisson's ratio, respectively. Using the relation between the covariant and the twisted bases and after simplifications, it can be checked that the elasticity tensor components in the twisted basis are given by:

$$C_{\alpha\beta\delta\gamma} = \frac{\nu E}{(1+\nu)(1-2\nu)}\delta_{\alpha\beta}\delta_{\delta\gamma} + \frac{E}{2(1+\nu)}(\delta_{\alpha\delta}\delta_{\beta\gamma} + \delta_{\alpha\gamma}\delta_{\beta\delta}), \tag{12}$$

where greek subscripts $\{\alpha, \beta, \gamma, \delta\}$ denote components x, y, Z in the twisted basis. The above expression coincides with the one obtained in the Cartesian basis, as the twisted basis is orthonormal.

3. Translational invariance

Translational invariance is a key property for applying the homogenization theory. For cylindrical structures, translational invariance means that both the cross-section and the material properties do not vary along the axis. For curved structures, there is another condition which states that the differential operator coefficients must not depend on the axial variable (Treyssède (2011)). As a consequence, for helical structures, the translational invariance requires the following three conditions (Treyssède (2008), Treyssède and Laguerre (2010)):

1. The material properties do not vary along the Z-axis in the twisted coordinate system;

2. The coefficients of the differential operators (gradient, divergence, Laplacian, ...) are independent on the axial variable Z;

3. The cross-section does not vary along the Z-axis in the twisted coordinate system.

Throughout this work, the material is assumed to be homogeneous and isotropic. In this case, the first condition is verified. To satisfy the second condition, it is sufficient to prove that the Christoffel symbols do not depend on the axial variable Z, which has been verified in the last section (see Eq. 8). Thus it remains only to verify the third condition.

Let us consider a helical single wire structure. The cross-section shape in the $(\mathbf{e}_X, \mathbf{e}_Y)$ plane at the axial position Z_1 is similar to that given at the position Z_2: there only exists a rotation of angle $2\pi(Z_2 - Z_1)/L$ around the Z-axis between these two cross-section shapes. Moreover, because the twisted basis plane $(\mathbf{e}_x, \mathbf{e}_y)$ also rotates around Z, the cross-section indeed remains fixed in this plane. Therefore, the translational invariance is checked for helical single wire structures. Fig. 2 shows the cross-section of four helical single wires with $R = 2a$ and different helical angles in the $(\mathbf{e}_X, \mathbf{e}_Y)$ plane. a is the radius of the circular cross-section (the cross-section being circular in the plane normal to the helical curve). Note that for small angle Φ, the cross-section shape in this plane is nearly circular because the structure is close to a cylinder (Fig. 2a). However the cross-section shape deviates from the circular one as Φ increases.

Let us now consider multi-wire helical structures. They are composed of a stack of helical wires, wrapped around a straight wire. A seven-wire strand is a special case of helical multi-wire structures containing one layer of six helical wires wrapped around the central wire. In the twisted basis, a cylindrical structure of axis Z with isotropic material is translationally invariant for any value of the torsion τ (see Treyssède and Laguerre (2010)). It therefore remains fixed in the Cartesian as in the twisted coordinate systems. The central wire is hence translationally invariant. As shown for helical single wire, the peripheral helical wires, which have the same helix parameters are also translationally invariant in the twisted coordinate system. The geometric invariance is then verified

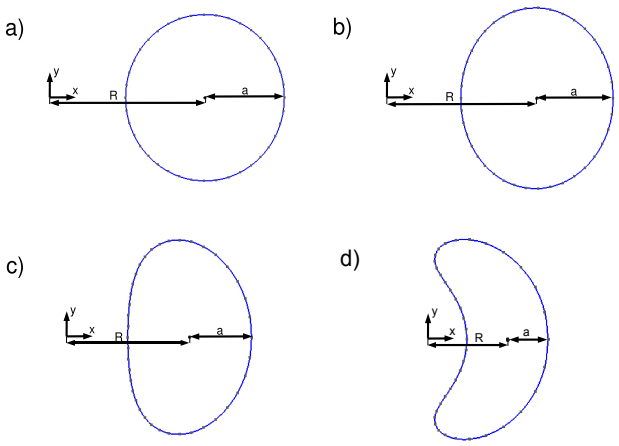

Figure 2: Cross-section of helical wires, $R/a = 2$ and (a) $\Phi = 10°$, (b) $\Phi = 30°$, (c) $\Phi = 50°$, (d) $\Phi = 70°$.

for the seven-wire strand in the twisted coordinate system and the problem is translationally invariant.

Let us briefly examine more complex structures. In multi-layer wire ropes, more than one layer of helical wires is present. Translational invariance in such structures is still satisfied if the torsion of each wire remains identical. This implies that translational invariance is not fulfilled in case of cross-lay strands because the torsion can be positive or negative. This loss of invariance is obvious if one thinks of contact discontinuities between two layers of opposite torsion. Contact discontinuities also necessarily occur in double helical structures, composed of one central strand wrapped by several peripheral strands. Such double helical structures, sometimes referred to as IWRC (independent wire rope core), hence cannot fulfill translational invariance.

To conclude this section, let us define the cross-section boundary in the plane $Z = 0$. The surface boundary of a helical single wire with circular cross-section is described in the Serret-Frenet basis by the following position vector:

$$\mathbf{X}(x, y, s) = \mathbf{r}(s) + a\cos t\mathbf{e}_n(s) + a\sin t\mathbf{e}_b(s), \tag{13}$$

where $t \in [0; 2\pi]$. Substituting Eq. (2) into Eq. (13), the cross-section shape

parameterization in the $(\mathbf{e}_X, \mathbf{e}_Y)$ plane is:

$$\begin{cases} X(t) = (R - a\cos t)\cos(\eta a \sin t + \theta) + \\ \qquad \dfrac{L}{l} a \sin t \sin(\eta a \sin t + \theta) \\ Y(t) = (R - a\cos t)\sin(\eta a \sin t + \theta) + \\ \qquad \dfrac{L}{l} a \sin t \cos(\eta a \sin t + \theta) \end{cases}, \tag{14}$$

where $\eta = -4\pi^2 R/lL$. This curve has been used to plot the cross-sections on Fig. 2. It has also been used for the FE mesh generation in Section 6.

4. Helical homogenization procedure

In this work, helical structures are supposed to be subjected to external loads at its end sections. Moreover, only axial loads (traction and torsion) are considered. Targeted helical structures are helical springs and seven-wire strands.

As explained in introduction, the purpose of this paper is to propose an approach for obtaining the static stress state, which will be used in the second part of this paper as a prestress state, for a wave propagation analysis. This can be achieved efficiently using an homogenization method. This approach, based on the asymptotic expansion method, exploits the translational invariance property. Homogenization splits the initial 3D elasticity problem into 2D problems posed on the cross-section, and a 1D straight beam problem. The overall beam behavior is computed thanks to the solution of the 2D problems. This solution, combined with the solution of the beam problem, provides also the local stress state.

For the present work, let us consider a slender helical structure of axial length H (see Fig. 3), with a cross-section denoted S^ε. This structure occupies the configuration $\Omega^\varepsilon = S^\varepsilon \times [0, H]$. The boundary of Ω^ε is defined by $\partial\Omega^\varepsilon = \Gamma^\varepsilon \cup \Gamma_0^\varepsilon \cup \Gamma_H^\varepsilon$, with $\Gamma_0^\varepsilon = S^\varepsilon \times \{0\}$ and $\Gamma_H^\varepsilon = S^\varepsilon \times \{H\}$ the two end cross-sections of the helical structure and Γ^ε the cross-section boundary. This structure exhibits a small parameter ε, corresponding to the inverse of the slenderness ratio, i.e. the ratio between the diameter of the cross-section S^ε and the length H.

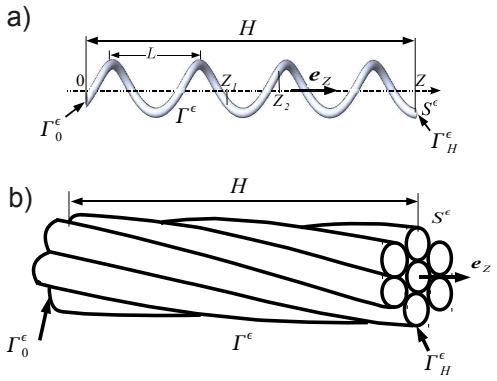

Figure 3: 3D helical structures. (a) single wire, (b) seven-wire strand.

4.1. The initial problem

The linear elasticity problem consists in finding the fields $\boldsymbol{\sigma}^\varepsilon$, $\boldsymbol{\epsilon}^\varepsilon$ and $\mathbf{u}^\varepsilon$, solution of:

$$\begin{cases} \nabla \cdot \boldsymbol{\sigma}^\varepsilon = \mathbf{0} \\ \boldsymbol{\sigma}^\varepsilon = \mathbf{C} \colon \boldsymbol{\epsilon}^\varepsilon(\mathbf{u}^\varepsilon) \\ \boldsymbol{\epsilon}^\varepsilon(\mathbf{u}^\varepsilon) = \nabla^s(\mathbf{u}^\varepsilon) \\ \boldsymbol{\sigma}^\varepsilon \cdot \mathbf{n} = \mathbf{0} \text{ on } \Gamma^\varepsilon \end{cases}, \tag{15}$$

where $\mathbf{C}$ is the elasticity tensor, which is supposed to be constant under the assumption of small displacements. $\nabla^s(\cdot)$ and $\nabla \cdot (\cdot)$ denote respectively the symmetric gradient (strain) and divergence operators. The solution must also verify the boundary conditions at the end sections. They are supposed to be under the form of stress data: $\boldsymbol{\sigma}^\varepsilon \cdot (-\mathbf{e}_Z) = \mathbf{t}^0$ on Γ_0^ε and $\boldsymbol{\sigma}^\varepsilon \cdot \mathbf{e}_Z = \mathbf{t}^H$ on Γ_H^ε, where $\mathbf{t}^0$ and $\mathbf{t}^H$ are the tractions at the end sections located at $Z = 0$ and $Z = H$. Moreover $\mathbf{t}^0$ and $\mathbf{t}^H$ are such that the overall structure equilibrium is fulfilled, which is a necessary condition for problem (15) to have a solution.

For seven-wire strand, the solution must verify Eq. (15) on each wire as well as contact equations, on the contact line between the central wire and each helical wire. This raises the problem of contact assumptions. In Ghoreishi et al. (2007), stick and slip conditions have been studied for computing the overall behavior. In Gnanavel and Parthasarathy (2011), an analytical model with

frictional contact was developed. Overall stiffness as well as maximum normal contact stresses were calculated from the authors's model and the Costello's model which assumes stick contact. In Argatov (2011) hypothesis of slip contact is made and maximum contact pressures (core-wire and wire-wire) were compared to FE computations performed with frictional contact in Jiang et al. (2008). All of these previous works have shown that the overall stiffness and contact stresses are very little sensitive to contact conditions. Therefore in this work, for simplicity, the contact is assumed to be stick. This amounts to perfect bonding conditions between wires: $\mathbf{u}_c = \mathbf{u}_p$ and $(\boldsymbol{\sigma} \cdot \mathbf{n})_c^+ + (\boldsymbol{\sigma} \cdot \mathbf{n})_p^- = 0$, where the subscripts c and p are related to the central and peripheral wires.

The solution of this problem (15) with boundary conditions and contact equations for multi-wire strand provides the prestress state. As mentioned previously, this problem may be computationally expensive to solve under this form, and the homogenization method aims to simplify it.

4.2. Asymptotic expansion method

To our knowledge very few works have been devoted to the asymptotic analysis of helical structures starting from a 3D formulation. We just mention Nicolet et al. (2007) in the framework of electrostatics. Therefore, the approach presented in this paper is based on Buannic and Cartraud (2000) and Buannic and Cartraud (2001a) developed for axially invariant and periodic beam-like structures respectively. More about asymptotic expansion method for slender structures may be found in some books (Sanchez-Hubert and Sanchez-Palencia (1992); Kalamkarov and Kolpakov (1997); Trabucho and Viaño (1996)).

The first step of the method consists in defining a problem equivalent to problem (15), but posed on a fixed domain that does not depend on the small parameter ε. A change of variables is thus introduced which takes into account the structure slenderness, in the twisted coordinates system: $(x, y, \zeta) = (x, y, \varepsilon Z)$. $\zeta = \varepsilon Z$ denotes the slow scale or macroscopic 1D-variable and $\{x, y\}$ denote the fast scale or microscopic 2D-variables. According to this change of variables,

the differential operators become

$$\begin{aligned} \nabla^s(.) &= \nabla^s_{xy}(.) + \varepsilon \nabla^s_\zeta(.) \ , \\ \nabla \cdot (.) &= \nabla_{xy} \cdot (.) + \varepsilon \nabla_\zeta \cdot (.) \ , \end{aligned} \tag{16}$$

where $\nabla^s_\zeta(.)$ and $\nabla_\zeta \cdot (.)$ correspond to partial differentiations with respect to the macroscopic variable ζ. $\nabla^s_{xy}(.)$ and $\nabla^s_{xy} \cdot (.)$ denote the differential operators with respect to the microscopic variables x and y.

Next, the displacement solution is searched under an asymptotic expansion form:

$$\mathbf{u}(\mathbf{x}) = u^0_x(\zeta)\mathbf{e}_x + u^0_y(\zeta)\mathbf{e}_y + \varepsilon \mathbf{u}^1(x,y,\zeta) + \varepsilon^2 \mathbf{u}^2(x,y,\zeta) + ... \tag{17}$$

In this expression, the translational invariance is taken into account since the k^{th}-order displacement $\mathbf{u}^k(x,y,\zeta)$ does not depend on the microscopic axial coordinate Z. Moreover, it is usually considered that the 0^{th}-order displacement has no axial component, which results from the property that for slender structures, the bending stiffness is much lower than axial stiffness. So 0^{th}-order displacement corresponds to a transverse deflection. Note that a proof of this result may be found in Trabucho and Viaño (1996) for homogeneous beams, and in Kolpakov (1991) for beams with periodic structure. As axial loads are considered in this work, and under the assumption that bending is not coupled with tension and torsion, this 0^{th}-order term vanishes.

Reporting expansion (17) in problem (15) with the use of (16), and considering ζ and $\{x, y\}$ as independent coordinates, one is led to a sequence of problems. On one hand 2D microscopic problems posed on the cross-section S, which will be denoted P^m_{2D}, where m denotes the order of ε in the equilibrium equation. On the other hand a sequence of 1D macroscopic problems will be also obtained, but only the lowest order macroscopic problem will be considered in the following.

4.3. Microscopic problems

The lowest order 2D microscopic problem posed on the cross-section S is P^1_{2D} with the following equations:

$$\begin{cases} \nabla_{xy} \cdot \boldsymbol{\sigma}^1 = 0 \\ \boldsymbol{\sigma}^1 = \mathbf{C} \colon \boldsymbol{\epsilon}^1 \\ \boldsymbol{\epsilon}^1 = \nabla^s_{xy}(\mathbf{u}^1) \\ \boldsymbol{\sigma}^1 \cdot \mathbf{n} = 0 \text{ on } \partial S \end{cases} . \tag{18}$$

It is important to notice that though this problem is 2D, the displacement $\mathbf{u}^1$ has three components. This results from the property than in a matrix form, from Eq. (10), one has:

$$\{\nabla^s_{xy}(\mathbf{u}^1)\} = \mathbf{L}_{xy}\{u^1\} = \mathbf{L}_{xy} \begin{Bmatrix} u^1_x \\ u^1_y \\ u^1_\zeta \end{Bmatrix} . \tag{19}$$

Problem P^1_{2D} is well-posed and has a unique solution up to a rigid body motion (Sanchez-Hubert and Sanchez-Palencia (1992); Buannic and Cartraud (2000)). The stress solution is obviously equal to zero. The displacement is thus a rigid body motion solution of $\nabla^s_{xy}(\mathbf{u}^1) = \mathbf{0}$, its expression in the twisted basis is:

$$\mathbf{u}^1 = u^1_\zeta(\zeta)\mathbf{e}_Z + \varphi^1(\zeta)[x\mathbf{e}_y - y\mathbf{e}_x], \tag{20}$$

corresponding to an overall translation u^1_ζ and rotation φ^1 around the Z-axis. The solution of problem (18) is then given by $\mathbf{u}^1$ with at this step arbitrary $u^1_\zeta(\zeta)$ and $\varphi^1(\zeta)$ and $\boldsymbol{\epsilon}^1 = \boldsymbol{\sigma}^1 = \mathbf{0}$.

The next order microscopic problem P^2_{2D} involves $\boldsymbol{\sigma}^2$, $\boldsymbol{\epsilon}^2$ and $\mathbf{u}^2$ solution of:

$$\begin{cases} \nabla_{xy} \cdot \boldsymbol{\sigma}^2 = 0 \\ \boldsymbol{\sigma}^2 = \mathbf{C} \colon \boldsymbol{\epsilon}^2 \\ \boldsymbol{\epsilon}^2 = \nabla^s_{xy}(\mathbf{u}^2) + \nabla^s_\zeta(\mathbf{u}^1) \\ \boldsymbol{\sigma}^2 \cdot \mathbf{n} = 0 \text{ on } \partial S \end{cases} . \tag{21}$$

Note that the displacement vector $\mathbf{u}^1$, obtained from the solution of the problem P^1_{2D}, appears through $\nabla^s_\zeta(\mathbf{u}^1)$ in P^2_{2D}. From Eq. (20), it can be seen

that the components of this strain tensor are, under a matrix form:

$$\{\nabla^s_\zeta(\mathbf{u}^1)\} = \left[\begin{array}{cccccc} 0 & 0 & E^E & 0 & -yE^T & xE^T \end{array}\right]^T , \tag{22}$$

where $E^E = \partial u^1_\zeta/\partial\zeta$ and $E^T = \partial\varphi^1/\partial\zeta$ and thus can be identified as macroscopic strains, i.e. extension and torsion respectively. Therefore, the other part of the strain $\nabla^s_{xy}(\mathbf{u}^2)$ is a microscopic strain.

Thanks to the problem linearity, its solution is a linear function of the macroscopic strains, up to a rigid body displacement which is of the form (20). So one has:

$$\begin{aligned} \mathbf{u}^2 = \boldsymbol{\chi}^E(x,y)E^E(\zeta) + \boldsymbol{\chi}^T(x,y)E^T(\zeta) + \\ u^2_\zeta(\zeta)\mathbf{e}_Z + \varphi^2(\zeta)[x\mathbf{e}_y - y\mathbf{e}_x] \, , \\ \boldsymbol{\sigma}^2 = \boldsymbol{\sigma}^E(x,y)E^E + \boldsymbol{\sigma}^T(x,y)E^T \, . \end{aligned} \tag{23}$$

As it will be shown in the next section, the lowest order macroscopic problem is a 1D beam problem, with extension and torsion. It thus involves macroscopic beam stresses which are simply defined from the integration over the cross-section S of the local or microscopic stresses $\boldsymbol{\sigma}^1$. Consequently the axial force T and the torque M take the form:

$$\begin{aligned} T(\zeta) &= \textstyle\int_S \sigma^2_{\zeta\zeta} dS \, , \\ M(\zeta) &= \textstyle\int_S (-y\sigma^2_{x\zeta} + x\sigma^2_{y\zeta}) dS \, , \end{aligned} \tag{24}$$

and from the solution of problem (21), one can define the overall beam behavior such that:

$$\left\{\begin{array}{c} T \\ M \end{array}\right\} = [k^{hom}] \left\{\begin{array}{c} E^E \\ E^T \end{array}\right\} , \tag{25}$$

where $[k^{hom}]$ is the stiffness matrix, which is symmetric.

4.4. Macroscopic problem

The lowest order macroscopic problem can be derived from compatibility conditions which express that problem (21) admits a solution, see e.g. Buannic and Cartraud (2000, 2001a). It amounts to integrate equilibrium equations of

problem (21) over the cross-section. This yields:

$$\left\{\begin{array}{l} dT/d\zeta = 0 \\ dM/d\zeta = 0 \\ \left\{\begin{array}{c} T \\ M \end{array}\right\} = [k^{hom}] \left\{\begin{array}{c} E^E \\ E^T \end{array}\right\} \\ E^E = \partial u_\zeta^1/\partial\zeta \\ E^T = \partial\varphi^1/\partial\zeta \end{array}\right. , \tag{26}$$

with boundary conditions at $\zeta = 0$ and $\zeta = \varepsilon H$. Since we have stress data for the 3D initial problem, and taking into account the overall equilibrium, these boundary conditions can be written as:

$$\left\{\begin{array}{l} T(0) = \int_S \mathbf{t}^0 \cdot (-\mathbf{e}_Z) dS \\ M(0) = \int_S (y\mathbf{t}^0 \cdot \mathbf{e}_x - x\mathbf{t}^0 \cdot \mathbf{e}_y) dS \\ T(\varepsilon H) = T(0) \\ M(\varepsilon H) = M(0) \end{array}\right. , \tag{27}$$

which corresponds to the application of the Saint-Venant principle, rigorously justified in the framework of asymptotic analysis of beams in Buannic and Cartraud (2001b).

The solution of this 1D macroscopic problem (26-27) is thus straightforward with a uniform macroscopic state: $T = T(0)$, $M = M(0)$, with the macroscopic strains E^E and E^T obtained from the inversion of (25) and u_ζ^1 and φ^1 calculated thanks to $(26)_{4-5}$ and defined up to a constant.

4.5. Summary

One can summarize the results of the asymptotic expansion method with the following expressions:

$$\begin{array}{c} \mathbf{u}(\mathbf{x}) = \varepsilon(u_\zeta^1(\zeta)\mathbf{e}_Z + \varphi^1(\zeta)[x\mathbf{e}_y - y\mathbf{e}_x]) + \\ \varepsilon^2(\boldsymbol{\chi}^E(x,y)E^E + \boldsymbol{\chi}^T(x,y)E^T + \\ u_\zeta^2(\zeta)\mathbf{e}_Z + \varphi^2(\zeta)[x\mathbf{e}_y - y\mathbf{e}_x]) + O(\varepsilon^3) , \\ \boldsymbol{\sigma} = \varepsilon(\boldsymbol{\sigma}^E(x,y)E^E + \boldsymbol{\sigma}^T(x,y)E^T) + O(\varepsilon^2) . \end{array} \tag{28}$$

It is recalled that microscopic fields $\boldsymbol{\chi}^E(x,y)$, $\boldsymbol{\chi}^T(x,y)$, $\boldsymbol{\sigma}^E(x,y)$ $\boldsymbol{\sigma}^T(x,y)$ are provided by the solution of the 2D microscopic problem (21) posed on the cross-section. Then, the expansions given in (28) can be easily computed up to the second-order rigid body motion, combining the previous solution of the 1D macroscopic problem with these microscopic fields.

5. Finite element solution

The variational formulation of the 2D microscopic problem (21) in the twisted coordinate system takes the form:

$$\forall \delta\mathbf{u}^2(x,y), \int_S \nabla^s_{xy}(\delta\mathbf{u}^2) : \boldsymbol{\sigma}^2 dxdy = 0, \tag{29}$$

and from Eq. $(21)_3$:

$$\boldsymbol{\sigma}^2 = \mathbf{C} : (\nabla^s_{xy}(\mathbf{u}^2) + \boldsymbol{\epsilon}_{macro}), \tag{30}$$

with $\boldsymbol{\epsilon}_{macro} = \nabla^s_\zeta(\mathbf{u}^1)$. Hence one has:

$$\begin{aligned} \forall \delta\mathbf{u}^2(x,y), \int_S \nabla^s_{xy}(\delta\mathbf{u}^2) : \mathbf{C} : \nabla^s_{xy}(\mathbf{u}^2) dxdy = \\ - \int_S \nabla^s_{xy}(\delta\mathbf{u}^2) : \mathbf{C} : \boldsymbol{\epsilon}_{macro} dxdy. \end{aligned} \tag{31}$$

We recall that $\{\nabla^s_{xy}(\mathbf{u}^2)\} = \mathbf{L}_{xy}\{u^2\}$, see (19). Then a finite element approximation of the form $\{u^2\} = [N^e]\{U^e\}$ is introduced , where $[N^e]$ is the matrix of shape functions, and $\{U^e\}$ the nodal displacements, with three degrees of freedom at each node. The variational formulation yields:

$$\begin{aligned} [K]\{U\} &= \{F\}, \\ [K^e] &= \int_{S^e} [N^e]^T \mathbf{L}^T_{xy} [C] \mathbf{L}_{xy} [N^e] dxdy, \\ \{F^e\} &= - \int_{S^e} [N^e]^T \mathbf{L}^T_{xy} [C] \{\epsilon_{macro}\} dxdy, \end{aligned} \tag{32}$$

with $[K]$ the stiffness matrix obtained from the assembly of element stiffness matrices $[K^e]$.

Note that in (32) the external load is given under the form of a macroscopic strain $\{\epsilon_{macro}\}$.

Once this system is solved, the stresses are computed thanks to (30) and after integration over the cross-section, the macroscopic beam stresses, i.e. the axial force and the torque are computed, thus providing the overall behavior $[k^{hom}]$.

6. Validation of the homogenization approach

In this section, the microscopic response is computed for helical springs and seven-wire strands under axial loading. The 2D FE model based on helical homogenization has been implemented in an in-house code. This model is first validated for helical springs by comparison with an analytical solution. Another validation is also presented for seven-wire strands with a reference solution obtained from a 3D FE model.

For helical single wire or multi-wire structures subjected to a given macroscopic extension E^E ($E^T = 0$), first the 2D model is generated. The cross-section is meshed, with six-node triangle elements to improve the geometrical description as well as results accuracy. The solution of the microscopic 2D problem is defined up to a rigid body displacement in the twisted coordinate system, see Eq. (20), which can be fixed by prescribing the axial displacement u_Z of an arbitrary node and the binormal displacement u_y of a node on the line $y = 0$. Then Eq. (32) is solved, and in the post-processing step, the computation of the axial force T and moment M are performed as well as the overall behavior.

6.1. Helical single wire structures

A helical single wire structure with circular cross-section is studied. R, Φ, n and a denote the helix radius, helix angle, number of helix pitches and the wire radius, respectively. Two types of structures can be distinguished: helical springs (large helix angle Φ and ratio R/a) and civil engineering cable (small angle Φ). The homogenization approach proposed in this paper is valid for any type of helical structures. However, in the literature, analytical solution is available only in the case of helical spring. Therefore, the validation of the homogenization approach is performed in that case.

The analytical solution may be found in Ancker and Goodier (1958). When one end-section is clamped while the other is subjected to axial load T with a fixed rotation, the axial deflection δ at its end is given by:

$$\begin{aligned} \delta &= \frac{4TR^3n}{Ga^4}\Psi, \\ \Psi &= 1 - \frac{3}{16}(\frac{a}{R})^2 + \frac{1}{(1+\nu)\tan^2\Phi}(\frac{1-\nu}{2} - \\ &\frac{\nu^2}{1+\frac{3-7\nu-20\nu^2-8\nu^3}{48(1+\nu)}(\frac{a}{R})^2+\frac{1+\nu}{\tan^2\Phi}}) + ..., \end{aligned} \tag{33}$$

where Ψ is a pitch and curvature correction factor.

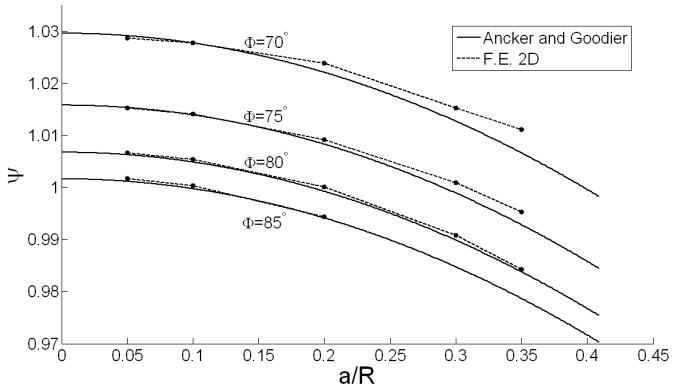

Figure 4: Correction factor Ψ vs. a/R for $\Phi = 70°, 75°, 80°, 85°$.

The inputs of the analytical solution are the ratio a/R, the helix angle Φ and the Poisson coefficient ν. For given geometric and material parameters, Eq. (33) is used to compute the correction factor Ψ.

The numerical results provided by the homogenization approach are compared with the analytical solutions for helical springs as follows. For a given δ, the macroscopic strain $E^E = \delta/nL$, $E^T = 0$ is imposed as the loading in (32) on the 2D FE model. Then the axial force T is computed. This leads

to a numerical value of Ψ according to Eq. $(33)_1$, which is compared to the analytical solution given by Eq. $(33)_2$. For $\nu = 0.3$, Fig. 4 shows the variation of the correction factor Ψ as a function of a/R for helix angle $\Phi = 70°$, $75°$, $80°$ and $85°$. Only small differences between numerical and analytical results can be seen for $a/R \leq 0.2$. This difference increases with a/R and as Φ decreases but remains less than 0.7% for $\Phi = 70°$ and $a/R = 0.35$, which is small.

The same evolution of the differences between the numerical results and the analytical solution was observed in Jiang et al. (2008), using a 3D FE model, with a free rotation. They are due to the non validity of the analytical model for large a/R and small helix angle Φ. However, our numerical results are in good agreement with those obtained from the analytical model providing a first validation of the computational homogenization approach.

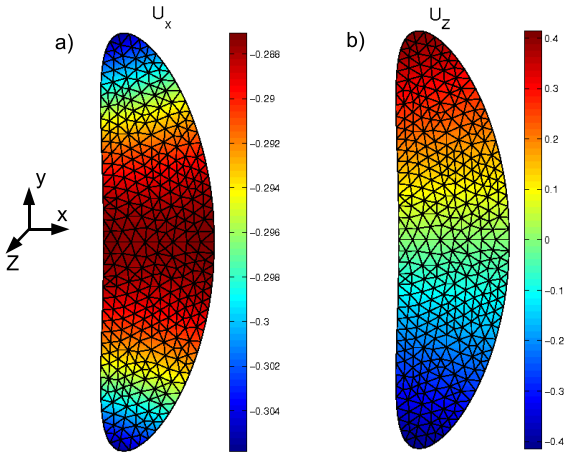

Figure 5: Dimensionless microscopic displacements in the cross-section of a helical spring ($R/a = 10$, $\Phi = 75°$) under axial deformation $E^E = 40\%$. (a) u_x^2/a, (b) u_ζ^2/a

Now, the 2D FE model is used to highlight the 3D microscopic displacements under extension. Fig. 5 shows the microscopic displacements $\mathbf{u}^2$ of helical spring with helix parameters $R/a = 10$ and $\Phi = 75°$ subjected to axial extension $E^E =$

40%. Note that this example corresponds to an extreme situation, where a large load is applied on helical spring with a small helix angle Φ. The mesh is made of 4327 dofs. It can be seen that axial displacement in Fig. 5(b) exhibits a linear evolution over the cross-section, which indicates the local bending response. For the geometrical and material properties $a = 2.7mm$, $\nu = 0.3$ and $E = 2e11Pa$, the computed axial force and torque are $T = 930.9N$ and $M = -1.83N.m$. This example will be used, in Part 2 of this paper, for the wave propagation analysis in prestressed elastic helical springs.

6.2. Seven-wire strands

Multi-wire cables form a large class of civil engineering components. Seven-wire strands, composed of one layer of helical wires wrapped around a central wire, are the basic element of these cables. The major advantage of the twisted structure is its ability to carry large loads.

The static behavior of seven-wire strands was studied among others in Ghoreishi et al. (2007) using a 3D FE model. In that paper the overall strand stiffness was identified from computations performed on a model of two pitch length, and these results are considered as reference results in the following.

The static behavior is computed using the computational homogenization approach and the 2D FE model. The 2D mesh is generated as follows: an independent mesh for each wire of the seven-wire strand is first considered. As mentioned before, the contact condition between the central and peripheral wires are assumed stick. Linear relations are then imposed at the contact point between the central and the peripheral wires, expressing the displacement continuity ($\mathbf{u}_c = \mathbf{u}_p$), where the subscripts c and p correspond to the central and peripheral wires, respectively. In practice, the system (32) is condensed to take into account these conditions.

As an example, Fig. 6 shows the mesh of the cross-section of a strand with the following parameters: central wire with radius a and helical wires with helix radius $R/a = 1.967$ and angle $\Phi = 7.9°$. The cross-section of the central straight wire is circular. As for the previous helical single wire structure, the

cross-section of helical wires is no longer circular in the $(\mathbf{e}_X, \mathbf{e}_Y)$ plane. Note that the helix radius R must be smaller than $2a$, otherwise the adjacent helical wires would overlap each other. This example will be considered later in this section as well as in Part 2.

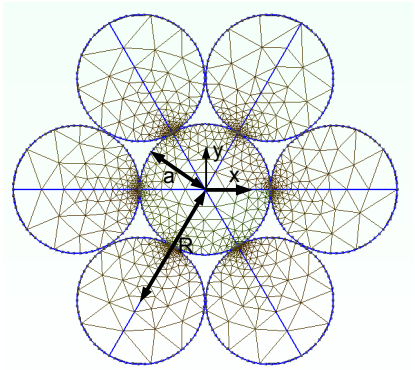

Figure 6: Mesh of seven-wire strand ($R/a = 1.967$, $\Phi = 7.9°$, a is the radius of the central wire)

Now, the overall behavior of seven-wire strand is computed. The stiffness components studied are the axial stiffness and the coupling between extension and torsion, i.e. the 11 and 21 components of the matrix $[k^{hom}]$ introduced in (25). In order to compare results obtained from the 2D FE model with the reference solution of Ghoreishi et al. (2007), we set $R/a = 2$, $\nu = 0.3$ and the stiffness components are written in the dimensionless form: $\overline{k}_{11} = k_{11}^{hom}/(E\pi R^2)$, $\overline{k}_{21} = k_{21}^{hom}/(E\pi R^3)$.

Fig. 7 displays the variation of the axial stiffness $\overline{k}_{11}$ as a function of the helix angle Φ, which varies between 2.5° and 35°. For $\Phi \leq 25°$, the difference between the two results is below 2%. This difference increases with Φ and reaches 10% for $\Phi = 35°$.

The variation of the coupling term $\overline{k}_{21}$ as a function of the helix angle Φ is shown in Fig. 8. For $\Phi \leq 8°$, the coupling term obtained by the two FE models are very close. For large helix angle, the difference between the two solutions is below 4%.

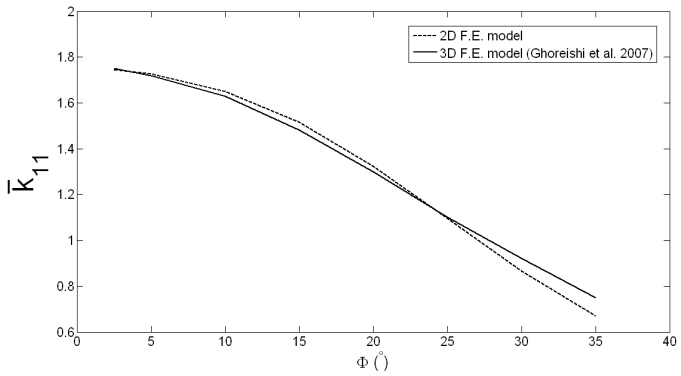

Figure 7: Dimensionless axial stiffness of seven-wire strand. $\overline{k}_{11}$ vs. Φ. $R/a = 2$.

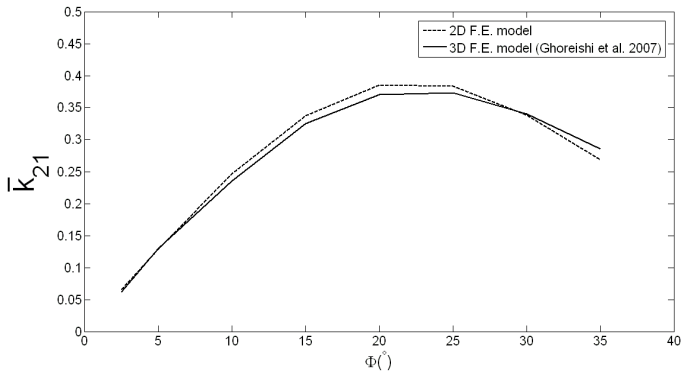

Figure 8: Dimensionless stiffness coupling term of seven-wire strand. $\overline{k}_{21}$ vs. Φ. $R/a = 2$.

The difference between the 2D and the reference 3D FE solutions can be explained by the use of a different mesh in the 2D model compared to the reference model. Indeed, the 2D mesh of a seven-wire strand with $\Phi = 5°$ use 1122 triangular elements and 2514 nodes, while the cross-section in the

reference 3D model is made of 72 elements and 210 nodes. Both the 2D and 3D FE models use quadratic elements. Moreover, an elliptical approximation of the cross-section shape was used in the 3D model, while the geometry is rigorously represented in the 2D model, according to Eq. (14). However as can be seen from Fig. (2), this approximation seems to be justified for examples studied with $\Phi \leq 35°$

Overall the macroscopic behavior of the seven-wire strand computed by the 2D FE model according to the homogenization approach is in good agreement with that obtained from the 3D model. This provides a second validation of the helical computational homogenization approach.

Lastly, microscopic displacements computed using the 2D FE model are analyzed. From the symmetry between the six helical wires, the displacements of only one peripheral wire is discussed. Fig. 9 shows the microscopic displacements in the cross-section of the seven-wire strand considered in Fig. 6 ($R/a = 1.967$, $\Phi = 7.9°$), subjected to $E^E = 0.6\%$. The in plane component u_x^2 of the central and the peripheral wire are shown in Fig. 9(a) and (c), respectively. One can observe the Poisson effect, with a linear evolution over the cross-section of u_x^2 in the central wire, and an affine evolution in the peripheral wire, which is maintained in contact with the central wire. The axial displacement is presented in Fig. 9(b) and (d) for the central and the peripheral wire, respectively. One can notice that for the central wire the microscopic axial displacement is close to zero except in the vicinity of contact points where small variations occur. In the helical wire, a linear evolution of the microscopic axial displacement over the cross-section is found, due to local bending. For this example, the core wire radius is $a = 2.7mm$ (the helical wire radius being $0.967a$). Material properties are: $\nu = 0.28$ and $E = 2.17e11Pa$. The computed axial force and torque are $T = 190.3kN$ and $M = 118.1N.m$. This example will used in Part 2 of this paper, for wave propagation analysis in prestressed strands.

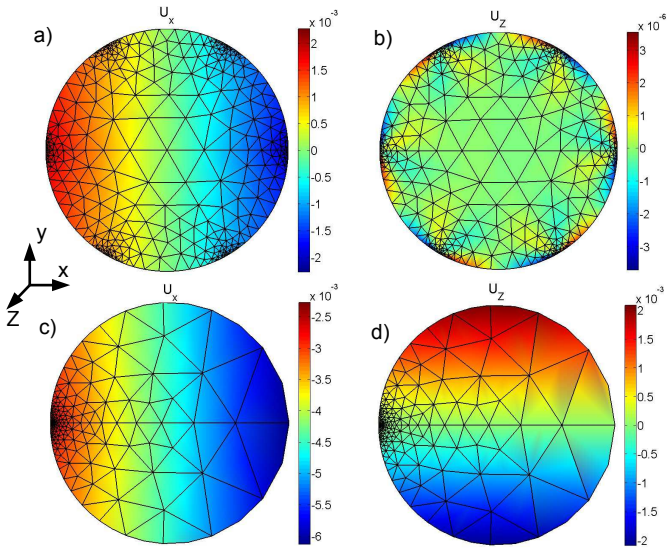

Figure 9: Dimensionless microscopic displacements of a seven-wire strand under axial deformation $E^E = 0.6\%$. (a) u_x^2/a and (b) u_ζ^2/a in the central wire (c) u_x^2/a and (d) u_ζ^2/a in the peripheral wire.

7. Conclusions

In this paper, the asymptotic expansion method has been applied to helical structures subjected to axial loads (traction and torsion) at its end sections. Thanks to the use of a twisted coordinate system, the 3D elastic problem has been reduced to a 2D microscopic problem posed on the cross-section and a 1D macroscopic beam problem, which has an analytical solution. Therefore the main contribution of this work is the derivation of the 2D microscopic problem, which fully exploits the translational invariance of the problem. The solution of this problem enables the computation of the overall beam stiffness as well as microscopic stresses corresponding to a given macroscopic loading. The proposed approach has been validated for helical single wire structures and seven-wire strands and compares favorably with reference analytical results or 3D FE computations.

In Part 2 of this paper, the solution of the microscopic problem is used in

order to take into account effects of prestress and geometry deformation on wave propagation.

References

Ancker, C.J., Goodier, J.N., 1958. Pitch and curvature corrections for helical springs. Journal of Applied Mechanics , 466–470.

Argatov, I., 2011. Response of a wire rope strand to axial and torsional loads: Asymptotic modeling of the effect of interwire contact deformations. International Journal of Solids and Structures 48, 1413–1423.

Bajas, H., Durville, D., Ciazynski, D., Devred, A., 2010. Numerical simulation of the mechanical behavior of iter cable-in-conduit conductors. IEEE Transactions on Applied Superconductivity 20, 1467–1470.

Boso, D.P., Lefik, M., Schrefler, B.A., 2006. Homogenisation methods for the thermo-mechanical analysis of nb3sn strand. Cryogenics 46, 569–580.

Buannic, N., Cartraud, P., 2000. Higher-order asymptotic model for a heterogeneous beam, including corrections due to end effects, in: Proc. of 41st AIAA/ASME/ASCE/AHS/ASC Structures, Structural Dynamics, and Materials Conference.

Buannic, N., Cartraud, P., 2001a. Higher-order effective modelling of periodic heterogeneous beams - Part 1: Asymptotic expansion method. International Journal of Solids and Structures 38, 7139–7161.

Buannic, N., Cartraud, P., 2001b. Higher-order effective modelling of periodic heterogeneous beams - Part 2: Derivation of the proper boundary conditions for the interior asymptotic solution. International Journal of Solids and Structures 38, 7163–7180.

Cartraud, P., Messager, T., 2006. Computational homogenization of periodic beam-like structures. International Journal of Solids and Structures 43, 686–696.

Chapelle, D., Bathe, K.J., 2003. The Finite Element Analysis of Shells-Fundamentals. Springer.

Costello, G.A., 1977. Theory of Wire Rope. Springer.

Durville, D., 1998. Modélisation du comportement mécanique de câbles métalliques. Revue Européenne des Eléments Finis 7, 9–22.

Erdönmez, C., İmrak, C.E., 2011. New approaches for model generation and analysis for wire rope. in Computational Science and Its Applications - ICCSA 2011, Lecture Notes in Computer Science, B. Murgante, O. Gervasi, A. Iglesias, D. Taniar, B. Apduhan editors, Springer , 103–111.

Ghoreishi, S.R., Messager, T., Cartraud, P., Davies, P., 2007. Validity and limitations of linear analytical models for steel wire strands under axial loading, using a 3d fe model. International Journal of Mechanical Sciences 49, 1251–1261.

Gnanavel, B., Parthasarathy, N., 2011. Effect of interfacial contact forces in radial contact wire strand. Archive of Applied Mechanics 81, 303–317.

Gray, A., Abbena, E., Salamon, S., 2006. Modern Differential Geometry of Curves and Surfaces with Mathmatica. 3rd Edition, Chapman and hall, Boca Raton.

İmrak, C.E., Erdönmez, C., 2010. On the problem of wire rope model generation with axial loading. Mathematical and Computational Applications 15, 259–268.

Jiang, W.G., Henshall, J.L., 2000. A novel finite element model for helical springs. Finite Elements in Analysis and Design 35, 363–377.

Jiang, W.G., Warby, M.K., Henshall, J.L., 2008. Statically indeterminate contacts in axially loaded wire strand. European Journal of Mechanics A/Solids 27, 69–78.

Jiang, W.G., Yao, M.S., Walton, J.M., 1999. A concise finite element model for simple straight wire rope strand. International Journal of Mechanical Sciences 41, 143–161.

Jolicoeur, C., Cardou, A., 1991. A numerical comparison of current mathematical models of twisted wire cables under axisymmetric loads. Journal of Energy Resources Technology 113, 241–249.

Kalamkarov, A.L., Kolpakov, A.G., 1997. Analysis, Design and Optimization of Composite Structures. Wiley.

Kolpakov, A.G., 1991. Calculation of the characteristics of thin elastic rods with a periodic structure. J. Appl. Math. Mech. 55, 358–365.

Messager, T., Cartraud, P., 2008. Homogenization of helical beam-like structures: application to single-walled carbon nanotubes. Computational Mechanics 41, 335–346.

Nawrocki, A., Labrosse, M., 2000. A finite element model for simple straight wire rope strands. Computers and Structures 77, 345–359.

Nemov, A.S., Boso, D.P., Voynov, I.B., Borovkov, A.I., Schrefler, B.A., 2010. Generalized stiffness coefficients for iter superconducting cables, direct fe modeling and initial configuration. Cryogenics 50, 304–313.

Nicolet, A., Movchan, A.B., Geuzaine, C., Zolla, F., Guenneau, S., 2007. High order asymptotic analysis of twisted electrostatic problems. Physica B: Condensed Matter 394, 335–338.

Nicolet, A., Zola, F., 2007. Finite element analysis of helicoidal waveguides. Measurement and Technology 28, 67–70.

Nicolet, A., Zola, F., Guenneau, S., 2004. Modeling of twisted optical waveguides with edge elements. The European Physical Journal Applied Physics 28, 153–157.

Onipede, O., Dong, S.B., 1996. Propagating waves and end modes in pretwisted beams. Journal of Sound and Vibration 195, 313–330.

Páczelt, I., Beleznai, R., 2011. Nonlinear contact-theory for analysis of wire rope strand using high-order approximation in the fem. Computers and Structures 89, 1004–1025.

Sanchez-Hubert, J., Sanchez-Palencia, E., 1992. Introduction aux méthodes asymptotiques et l'homogénéisation. Masson, Paris.

Stanova, E., Fedorko, G., Fabian, M., Kmet, S., 2011a. Computer modelling of wire strands and ropes part i: Theory and computer implementation. Advances in Engineering Software 42, 305–315.

Stanova, E., Fedorko, G., Fabian, M., Kmet, S., 2011b. Computer modelling of wire strands and ropes part ii: Finite element-based applications. Advances in Engineering Software 42, 322–331.

Synge, J.L., Schild, A., 1978. Tensor Calculus. Dover.

Trabucho, L., Viaño, J.M., 1996. Mathematical modelling of rods. Handbook of Numerical Analysis IV, P.G. Ciarlet, J.L. Lions editors, North-Holland , 487–974.

Treyssède, F., 2008. Elastic waves in helical waveguides. Wave Motion 45, 457–470.

Treyssède, F., 2011. Mode propagation in curved waveguides and scattering by inhomogeneities: application to the elastodynamics of helical structures. Journal of the Acoustical Society of America 129, 1857–1868.

Treyssède, F., Laguerre, L., 2010. Investigation of elastic modes propagating in multi-wire helical waveguides. Journal of Sound and Vibration 329, 1702–1716.

Wahl, A.M., 1963. Mechanical Springs. Second Edition, Mc Graw-Hill, Inc., New York.

Wempner, G., 1981. Mechanics of Solids with Applications to Thin Bodies. Sijthoff and Noordhoff, The Netherlands.